

Soil moisture impacts on convective margins

BENJAMIN R. LINTNER AND J. DAVID NEELIN

Department of Atmospheric Sciences, and Institute of Geophysics and Planetary Physics, University of California, Los Angeles

(February 1, 2009)

ABSTRACT

An idealized prototype for the location of the margins of tropical land region convection zones is extended to incorporate the effects of soil moisture and associated evaporation. The impact of evaporation, integrated over the inflow trajectory into the convection zone, is realized nonlocally where the atmosphere becomes favorable to deep convection. This integrated effect produces “hotspots” of land surface-atmosphere coupling downstream of soil moisture conditions. Overall, soil moisture increases the variability of the convective margin, although how it does so is nontrivial. In particular, there is an asymmetry in displacements of the convective margin between anomalous inflow and outflow conditions which is absent when soil moisture is not included. Furthermore, the simple cases presented here illustrate how margin sensitivity depends strongly on the interplay of factors including net top-of-the-atmosphere radiative heating, the statistics of inflow wind, and the convective parameterization.

1. Introduction

As transition zones between strong and weak mean precipitation regimes, the margins of tropical land region convection zones experience significant variability. Interannually, some of the most severe droughts occur as localized spatial shifts in the margins of convection zones. Moreover, the tropical hydrologic cycle signatures of greenhouse gas-induced climate change as simulated by models are often strongly localized along particular convective margins, albeit with significant intermodel differences regarding precisely where such changes occur (Williams et al., 2001; Douville et al., 2002; Johns et al., 2003; Soden and Held, 2006; Neelin et al., 2006; IPCC, 2007; Chou et al., 2008).

Given the variability inherent to convective margins, there is a need for detailed mechanistic understanding of the factors controlling their behavior. In previous work, Lintner and Neelin (2007; hereafter LN07) developed a simple prototype to describe convective margins under idealized conditions of low-level dry air inflow into a land region from an adjacent ocean. The LN07 prototype demonstrates how the characteristics of such inflow convective margins, e.g., the location of the transition between nonconvecting and convecting conditions, depend on dynamic and thermodynamic variables, including low-level circulation, inflow moisture, and tropospheric temperature.

For simplicity, the LN07 analysis neglected effects of land surface conditions such as soil moisture on convective margins. Of course, the capacity of the land surface to retain moisture significantly influences the cli-

mate system. Soil moisture directly impacts surface-atmosphere energy fluxes through evaporation, which modulates the partitioning of the surface energy budget (Charney, 1975; Shukla and Mintz, 1982; Delworth and Manabe, 1988). Soil moisture further constrains vegetation, thereby impacting surface parameters like albedo and surface roughness that in turn affect surface radiative properties and turbulent exchanges of energy, moisture, and momentum (Xue and Shukla, 1993). The persistence of soil moisture on seasonal or longer timescales provides a source of memory to the climate system (Vinnikov et al., 1996), as do slowly-varying vegetation characteristics related to soil moisture (Delire et al., 2004; Notaro et al., 2006).

Much interest has focused on soil moisture’s influence on precipitation and its variability, especially the positive feedback through which anomalous precipitation conditions are self-sustained and amplified by the land surface state. The existence of such feedbacks has implications for predictability and long-range forecast skill, e.g., land-atmosphere interactions are thought to play a role in the persistence of drought conditions (Hong and Kalnay, 2000; d’Odorico and Porporato, 2004). Observational studies based on large-scale irrigation projects (Stidd, 1975; Barnston and Schickedanz, 1984; Moore and Rojstaczer, 2002), soil moisture field measurement networks (Findell and Eltahir, 1997 and 1999), and precipitation persistence statistics (Taylor et al., 1997; Taylor and Lebel, 1998; Taylor et al., 2003; Koster and Suarez, 2004) point to the operation of the soil moisture-precipitation feedback in nature. General cir-

ulation models (GCMs) also manifest the soil moisture-precipitation feedback (Atlas et al., 1993; Beljaars et al., 1996; Zheng and Eltahir, 1998; Pal and Eltahir, 2001, 2003; D’Odorico and Porporato, 2004), although fundamental questions remain regarding the feedback’s magnitude and sensitivity to model parameterizations (Koster et al., 2004; Dirmeyer et al., 2006; Wu et al., 2007; Steiner et al., 2008).

An emergent feature of the simulated soil moisture-precipitation feedback is the occurrence of hotspots, locations of strong land surface-atmosphere coupling (Koster et al., 2004; Guo et al., 2006; Notaro, 2008). Within the Tropics, such hotspots typically appear in the transition zones between the wettest and driest mean climates. Koster et al., (2004) stressed the role of soil moisture in producing locally intensified soil moisture-precipitation coupling. Within the driest regions, evaporation exhibits significant sensitivity to soil moisture but evaporation rates are small, with limited potential to affect precipitation. Within the wettest regions, soil moisture perturbations cause only small variations in evaporation, since the sensitivity of evaporation to soil moisture diminishes as the surface approaches saturation. It is between the wettest and driest extremes that soil moisture perturbations are most conducive to driving variations in precipitation.

Although the role of atmospheric dynamics and convection is inherent in this view of hotspots, the focus of the present study is to elucidate the atmospheric side of land-atmosphere coupling. In particular, we consider circumstances under which the large-scale inflow air mass characteristics into a land region convection zone modulate precipitation along the convective margin, with an emphasis on diagnosing the interplay of margin variability and the underlying surface conditions. Since our principal objective is to develop insights into soil moisture influences on convective margin variability, we develop analytic prototypes that are intended to illustrate some basic mechanisms. We also employ an intermediate level complexity model coupled to a simplified land surface scheme. What this model lacks in terms of realism is leveraged against the ease with which it can be analyzed and interpreted, although even the simple cases considered are nontrivial. We further explore the extent to which the results of this analysis may be applied to more complex models and observations.

2. Soil moisture impact inferred from an intermediate level complexity model

The model used is the Quasi-equilibrium Tropical Circulation Model 1 Version 2.3 (QTCM1; Neelin and Zeng, 2000; Zeng et al., 2000), an intermediate level com-

plexity model of the tropical troposphere. An advantage of QTCM1 over GCMs is the simplicity of the model framework: QTCM1’s transparency facilitates diagnosis in ways that are not always feasible or straightforward with GCMs. The simplicity of QTCM1 has proved useful for elucidating many tropical climate phenomena, including tropical ocean-atmosphere coupling (Su et al., 2003), El Niño/Southern Oscillation (ENSO) tropical teleconnections (Neelin and Su, 2005), climate sensitivity to global warming (Chou and Neelin, 2004), intraseasonal variability (Lin et al., 2000), monsoons (Chou and Neelin, 2003), and vegetation-atmosphere interactions (Zeng et al., 1999).

The QTCM1 simulations considered here represent the land surface moisture through a simple bucket model (Zeng et al., 2000), with evaporation E linearly proportional to potential evaporation E_p , i.e., $E = \beta(w)E_p$, where the evaporation efficiency $\beta(w)$ is a function of the soil wetness w . The latter is a dimensionless quantity obtained by normalizing the soil moisture content by the soil moisture holding capacity w_0 ; w ranges between 0 and 1, with $w = 0$ ($= 1$) representing a completely desiccated (saturated) surface, although w effectively maximizes at values < 1 because of constraints imposed by atmospheric and surface energy balances. In our implementation, $\beta(w) = w$ and $w_0 = 150$ mm unless otherwise stated. The total surface runoff is modeled as $w^\gamma P$, where P is precipitation and $\gamma = 4$. Although the bucket model neglects many features necessary to provide a fully realistic picture of land-atmosphere coupling (e.g., vegetation, partitioning of evaporation into transpiration and soil evaporation, plant rooting depth, multiple soil layers), it retains sufficient complexity to produce nontrivial behavior.

We consider first a set of experiments motivated by approaches to investigate soil moisture impacts in prior studies (e.g., Koster et al., 2004). In particular, we performed a control simulation (denoted CTL) and a sensitivity simulation in which $\beta(w)$ was fixed to a climatology that produces the same mean evaporation as in CTL, i.e., $\beta(w)^* = [\overline{\beta(w)} + \overline{\beta(w)'}E_p'/\overline{E_p}]_{CTL}$; the latter is denoted “FIXED- β ”. Here, overbars and primes denote time-means and deviations from time-means, respectively. Each simulation was forced with imposed climatological monthly-mean sea surface temperatures (SSTs), such that the variability present arises solely from QTCM1’s internal dynamics. The simulations were performed at a horizontal resolution of $1.40625^\circ \times 1^\circ$, with output saved as 5-day (pentadal) means for 25 years.

Figure 1a illustrates 3-month seasonal mean precipitation standard deviations of the CTL run, σ_P^{CTL} , for tropical South America (shaded contours). For comparison,

the seasonal mean climatologies (line contours) are also shown. In general, the largest variability occurs not at the highest mean rainfall (here $> 14 \text{ mm day}^{-1}$) but rather at somewhat lower values ($4 - 10 \text{ mm day}^{-1}$), i.e., along the convective margins. Note that the lack of interannually-varying SSTs means that important contributions to observed precipitation variability such as ENSO are absent in the QTCM1 simulations. A further caveat is that QTCM1, like many models, may overemphasize margin variability, since the model simulates too little variability in the interior of the convection zone (Lin et al., 2000).

The ratio of σ_P^{CTL} to the standard deviation of the FIXED- β simulation, $\sigma_P^{FIXED-\beta}$, provides a measure of the importance of interactive soil moisture variations to total precipitation variability in QTCM1 (Figure 1b; shaded contours). Generally, the largest increases of precipitation variability by interactive soil moisture are localized to the convective margins, although there is considerable spatial variation in the effect. However, the geographic distribution of soil moisture amplification of precipitation variability over tropical South America is broadly consistent with the pattern of soil moisture-precipitation coupling hotspots evident in prior studies (c.f., Figure 1 of Koster et al., 2004 for a comparison to JJA). Other regions of strong soil moisture-precipitation coupling in QTCM1 include the Sahel region of Africa and northern Australia (not shown). QTCM1's ability to simulate hotspots means that the model has some utility in diagnosing hotspot genesis, as discussed in Section 5. In the following section, we employ an analytic prototype to address modifications to convective margin behavior in the presence of soil moisture and evaporation.

3. Incorporating evaporation into the convective margins framework

a. Set-up

As in LN07, we consider 1D steady-state, vertically-integrated tropospheric temperature (T) and moisture (q) equations applied to a land region lying to the west of an ocean region, as is the case over northeastern South America (Figure 2; see Section 6 for discussion of caveats to applicability of the prototype to this region):

$$M_s \nabla \cdot \mathbf{v} = P + R_{surf} + R_{toa} + H \quad (1)$$

$$-(M_{qp}q) \nabla \cdot \mathbf{v} = -u_q \partial_x q + E - P \quad (2)$$

Here R_{surf} and R_{toa} are the net surface and top-of-the-atmosphere shortwave plus longwave radiative heating, respectively; E is latent heat flux (evapotranspiration); H is sensible heat flux; and P represents convective heating in (1) or drying in (2). For T and q in units

of K (the latter by absorbing the ratio of latent heat of condensation, L , to heat capacity at constant pressure, c_p) the radiative, turbulent heating, and convective fluxes are dimensionalized to K s^{-1} (normalizing by $c_p \Delta p g^{-1}$, where Δp is the tropospheric pressure depth and g is acceleration due to gravity). The terms on left-hand side of each equation are related to vertical heat and moisture flux convergence, with $\nabla \cdot \mathbf{v}$ (units of s^{-1}) related to the convergence of the flow (signed positive for conditions of low-level convergence) and M_s and $M_q = M_{qp}q$ (K) are dry static stability and moisture stratification, respectively (Yu et al., 1998). The first term on the right-hand side of (2) is the horizontal moisture advection, with u_q (m s^{-1}) the projection of the windfield onto the vertical structure of q . A comparable term in the temperature equation is neglected as horizontal temperature gradients are assumed to be weak (Sobel and Bretherton, 2000).

Adding (1) and (2) and invoking a zero net surface flux constraint, $R_{surf} + E + H = 0$, yield an expression for the horizontal convergence, i.e.,

$$\nabla \cdot \mathbf{v} = M^{-1} [R_{toa} - u_q \partial_x q] \quad (3)$$

which upon substitution into the moisture equation (2) yields:

$$P = E - u_q \partial_x q (1 + M_{qp}q/M) + M_{qp}q R_{toa}/M \quad (4)$$

Here, $M = M_s - M_{qp}q$ denotes the gross moist stability.

For nonconvecting regions, with $P = 0$, it is instructive to consider instead

$$\nabla \cdot \mathbf{v}_{nc} = M_s^{-1} [R_{toa} - E] \quad (5)$$

The nonconvecting region moisture equation is then:

$$u_q \partial_x q = M_{qp}q M_s^{-1} [R_{toa} - E] + E \quad (6)$$

From (6), it can be seen that E has two effects that tend to cancel. On the one hand, $E > 0$ corresponds to a source of tropospheric moisture, while on the other, $E > 0$ offsets the effect of net energy input at the top of the atmosphere ($R_{toa} > 0$), reducing $\nabla \cdot \mathbf{v}_{nc}$. Combining the terms in E shows the effective contribution of E is scaled by a factor of $(1 - M_{qp}q M_s^{-1}) = M M_s^{-1}$.

For the idealized steady-state convective margin solution of LN07, E in the nonconvecting portion of the domain was set to zero, since $w = 0$ in the absence of recharge by precipitation. However, realistic situations for which E is nonzero are encountered on seasonal or subseasonal timescales, as with the annual cycle movements of land region convection zones, since the decay time for w is of order a few months.

b. *Shift of the convective margin associated with an imposed evaporation in the nonconvecting region*

It is notationally convenient to recast (6) as

$$\partial_x q - \lambda_E(x)q = u_q^{-1}E \quad (7)$$

where

$$\lambda_E(x) = M_{qp}(M_s u_q)^{-1}[R_{toa} - E] \quad (8)$$

$\lambda_E(x)$, which is in units of length^{-1} , can be interpreted as the local spatial rate of moisture increase along an inflow trajectory associated with moisture convergence.

For arbitrary $R_{toa}(x)$ and $E(x)$, integrating (7) between the inflow position (at x_0) and x yields:

$$q(x) = e^{\Lambda(x)}[q(x_0) + \int_{x_0}^x e^{-\Lambda(x')}u_q^{-1}E(x')dx'] \quad (9)$$

where $\Lambda(x) = \int_{x_0}^x \lambda_E(x')dx'$. The second term in brackets on the right-hand side of (9) represents the spatially-integrated effect of evaporation across the nonconvecting region. For illustrative purposes, taking $R_{toa}(x)$ and $E(x)$ as constants in the nonconvecting region, (9) yields (setting $x_0 = 0$),

$$q(x) = (q_0 + q_E)e^{\lambda_E x} - q_E \quad (10)$$

where q_0 is the inflow specific humidity and $q_E = (u_q \lambda_E)^{-1}E = M_s E / M_{qp}(R_{toa} - E)$ is a moisture scale associated with evaporation and convergence. If $E > R_{toa}$, leading to divergence in (5), the moisture scale associated with q_E (with sign reversed) represents the value of moisture for which evaporation and moisture divergence balance, with the inflow q_0 decaying toward it. On the other hand, under conditions with $E < R_{toa}$, moisture increases exponentially along the inflow trajectory. We point out that q_E increases moisture along the inflow trajectory; however, λ_E is smaller, relative to no-evaporation conditions, which reduces q . This behavior reflects the compensation between moistening directly associated with E and lowered convergence indirectly associated with changes to column flux forcing.

For a temperature-dependent convective threshold condition in moisture $q_c(T)$, the convective margin occurs at:

$$x_c^E = \lambda_E^{-1} \ln[(q_c(T) + q_E)/(q_0 + q_E)] \quad (11)$$

As illustrated in Figure 3a, for a given R_{toa} , x_c^E decreases as E increases, i.e., the margin shifts closer to the inflow point. The displacement of the margin toward the inflow point implies that the direct moistening effect associated with q_E dominates over the convergence reduction in λ_E . In terms of the dependence of (11) on

top-of-the-atmosphere radiative heating, as R_{toa} is increased, x_c^E moves closer to the inflow point, since larger R_{toa} enhances vertical moisture convergence. Further, Figure 3b shows stronger sensitivity of x_c^E to the inclusion of evaporation with E small, with larger sensitivity of x_c^E to E perturbations for a given value of E when R_{toa} is small. Note that while the value of q_E becomes large as $R_{toa} \rightarrow E$, the value of x_c^E becomes large as $R_{toa} \rightarrow -M_{qc}M_s^{-1}E$, where $M_{qc} = M_{qp}q_c(T)$.

Based on these results, convective margin sensitivity to E in models or observations should be strongly affected by the relative values of R_{toa} and E . Moving poleward from the Tropics, R_{toa} varies as a result of the latitudinal variation in top-of-the-atmosphere insolation; in the winter hemisphere, or during the equinoctial seasons, the meridional decrease of top-of-the-atmosphere insolation causes R_{toa} to become small and, at some latitude, to change sign. (Such latitude dependence is roughly analogous to the x-axis in Figure 3a.) With the caveats that (11) strictly applies to steady-state conditions and simplified inflow geometries, increased margin sensitivity is anticipated to occur at particular locations dictated by the interplay of the various control factors.

c. *Asymmetric displacements of the convective margin under anomalous windfield perturbations*

Having considered the mean margin shift that occurs with inclusion of evaporation, we now discuss the related issue of margin variations to imposed windfield perturbations δu_q in the presence of nonzero E . The starting point is the mean state of LN07, with $E(x) = 0$ outside of the convecting region ($x < x_c^0$) and $E(x) = E$ inside ($x > x_c^0$).

For anomalous outflow ($\delta u_q < 0$), the low-level wind perturbation induces the margin to move toward the inflow point, over a dry surface. The solution is thus identical to LN07, but with $u_q \rightarrow u_q + \delta u_q$; thus,

$$\delta x_c = (\delta u_q / u_q) \lambda_0^{-1} \ln(q_c / q_0) \quad [\text{outflow}] \quad (12)$$

For anomalous inflow ($\delta u_q > 0$), by contrast, the margin will be shifted away from the inflow point, over a residually wet surface. From (9), it can be shown that

$$\delta x_c = (1 + \delta u_q / u_q) \lambda_E^{-1} \ln \left[\frac{1 + q_E / q_c}{(q_0 / q_c)^{\delta u_q / (u_q + \delta u_q)} + q_E / q_c} \right] \quad [\text{inflow}] \quad (13)$$

In the limit $\delta u_q / u_q \rightarrow 0$, (13) is, to first order in $\delta u_q / u_q$,

$$\delta x_c \approx x_c^0 (\delta u_q / u_q) \frac{1}{1 + (M_s - M_{qc})E / (M_{qc} R_{toa})} \quad [\text{inflow}] \quad (14)$$

Equation (14) resembles (12), but modified by a factor of $\kappa = [1 + (M_s - M_{qc})E / (M_{qc} R_{toa})]^{-1}$. Since the second

term in κ is positive, $\kappa < 1$, which means that for δu_q of given magnitude, the x_c displacements for anomalous inflow conditions are smaller than for anomalous outflow conditions. Such asymmetric displacements arise from the distinct surface states encountered under inflow and outflow perturbations: with the former air masses approaching the convective margin interact with a wet surface near the margin, which enhances the moisture loading of the inflow relative to what it would be upon transiting over a dry surface. The residual moistening allows q_c to be met earlier along the inflow trajectory. For typical (QTCM1) values of E , R_{toa} , M_{q_c} , and M , $\kappa \approx 0.5-0.75$.

d. Timescale for margin adjustment

The prototype effectively assumes time-independent surface states; in reality, the surface adjusts to the margin displacement, e.g., the initially wet surface encountered under anomalous inflow conditions will begin to dry as evaporative demand diminishes soil wetness. The timescale for margin adjustments, τ_{margin} , is approximately $|\delta x_c/u_q| \approx |\delta u_q/u_q| \frac{M_s \ln(q_c(T)/q_0)}{M_{qp}(R-E)}$, which is of order $30|\delta u_q/u_q|$ days for the configuration discussed in the next section. On the other hand, the evaporative timescale, τ_E , is approximately $\frac{Lw_0}{E_p}$, assuming constant potential evaporation. For E_p of order 100 Wm^{-2} , and $w_0 = 150 \text{ mm}$, $\tau_E \approx 45$ days. For wind perturbations such that $30|\delta u_q/u_q| \ll 45$ days, the margin will effectively adjust before the surface state is substantially altered. At lower (e.g., seasonal) frequencies, the surface evolution may play a role, as considered in Section 6. Also, for regions where $R_{toa} \rightarrow E$, τ_{margin} becomes large, so that the atmospheric adjustment timescale may become non-negligible compared to τ_E .

4. Implications of soil moisture for high-frequency variability of the convective margin

a. Idealized QTCM1 configuration

In this section, the results of several idealized QTCM1 simulations designed specifically to provide insights into soil moisture impacts on convective margins are discussed. The model set-up here consists of an equatorial, zonal strip half occupied by a single ocean and land region. For the ocean region, uniform SST was imposed. Top-of-the-atmosphere insolation and surface albedo values were set to equinoctial conditions along the equator. In each simulation discussed below, the tropospheric temperature is a prescribed constant.

Under steady state conditions, the idealized QTCM1 tropical strip simulation yields a single convection zone

symmetric about the mid-point of the land region. To generate variations in the convection zone, spatially-uniform, Gaussian-distributed stochastic wind perturbations were imposed in the model's moisture advection scheme. For computational and diagnostic simplicity, the perturbations were added to the barotropic component of the total windfield over 10-day intervals. The perturbation timescale, while long compared to typical observed tropical transient timescales (such as easterly waves), was chosen to allow the margin in the idealized tropical strip configuration some time to adjust, thereby diminishing the effect of initial conditions on the margin response.

The perturbation precipitation profile, averaged over 500 perturbations, appears in Figure 4 (solid red line; hereafter, we refer to this simulation as “ δCTL ”). Note that the x -coordinate has been normalized relative to the non-perturbed precipitation profile: $x = 1$ corresponds to x_c^E in the steady state, defined relative to the land-ocean interface at $x = 0$. The principal impact of the imposed perturbations is a smoothing of the precipitation profile: the imposed perturbations essentially displace the edge of the convection zone back and forth, such that for the mean over a large number of perturbations, a smoothly tapered profile emerges.

b. Fixed β and no wetness memory experiments

To demonstrate how soil moisture impacts the variability of the convective margin, two sensitivity experiments were conducted. One sensitivity case ($\delta\text{FIXED-}\beta$) implemented fixed β conditions, with β estimated (as in Section 2) from δCTL . The other ($\delta\text{NOWETMEM}$) used E estimated functionally from P at each land grid-point through a 6th-order polynomial fit between the mean E and P fields obtained from δCTL . This “no wetness memory” simulation suppresses residual soil moisture anomalies associated with prior precipitation conditions and is effectively equivalent to $w_0 \rightarrow 0$.

Under fixed β conditions, there is little impact on the mean precipitation profile (Figure 4; solid blue line); however, the standard deviation, $\sigma_P^{\delta\text{FIXED-}\beta}$ (dashed blue line), is reduced by 20%. For $\delta\text{NOWETMEM}$, the mean precipitation profile (green line) is lowered in the transition to the strongest precipitation values. This mean change can be understood in the context of the prototype results of Section 3b: by eliminating residual soil moisture outside of the convection zone—and thus any evaporative moistening from the surface—the mean $\delta\text{NOWETMEM}$ inflow into the convection zone is drier compared to either δCTL or $\delta\text{FIXED-}\beta$, resulting in reduced mean precipitation values near the convective margin. $\sigma_P^{\delta\text{NOWETMEM}}$ (dashed green line) is

enhanced relative to $\sigma_P^{\delta CTL}$, especially on the strongly-convecting side of the profile.

c. Anomalous inflow/outflow asymmetry

For the no wetness memory simulation, nonzero E occurs locally during a particular model timestep only if P is nonzero at the same location during that timestep. If P ceases—as, for example, when the windfield perturbation shifts the convective margin—the soil moisture impact (and hence E) is instantaneously removed. Relative to δCTL , an inflow windfield perturbation of given magnitude results in a greater westward margin displacement in $\delta NOWETMEM$, since the effect of residual w outside of the convecting region is eliminated. Figure 5a, which displays x_c values bin-averaged by the windfield perturbations, δu_0 , underscores this behavior, as the x_c values in δCTL (red) lie below the $\delta NOWETMEM$ values (green) for $\delta u_0 > 0$. For $\delta FIXED-\beta$, the x_c values for $\delta u_0 > 0$ also lie below those of $\delta NOWETMEM$ (blue). However, the scatter in the δu_0-x_c relationship for fixed β conditions is attenuated relative to δCTL . The change in x_c variability points to modulation of the margin location by time-dependent soil moisture perturbations.

Comparing the idealized QTCM1 results to the analytic prototype of Section 3 demonstrates favorable agreement. Assuming no effect from soil moisture (or evaporation) outside of the convection zone, the analytic solution (black) closely matches $\delta NOWETMEM$, although the slope of the predicted δu_0-x_c relationship is a little too steep. This discrepancy is largely attributed to non-leading order spatial structure neglected in the analytic solution, e.g., R_{toa} and M_s are not strictly uniform. When the effect of residual E is included, the analytic slope (gray) is reduced for anomalous inflow conditions, with the value approximately matching the $\delta FIXED-\beta$ (or δCTL) results. It is worth reiterating that the analytic solutions are steady-state approximations while the numerical results have some time dependence associated with atmospheric adjustment and, for the δCTL simulation, the soil moisture.

As was noted in Section 3b, R_{toa} affects the sensitivity of the convective margin. Repeating the δCTL , $\delta FIXED-\beta$, and $\delta NOWETMEM$ simulations with R_{toa} reduced (by lowering net top-of-the-atmosphere insolation) underscores this sensitivity (Figure 5b). Much of the increased scatter in the δu_0-x_c relationship (as evidenced by larger standard errors) is associated with the lengthening of τ_{margin} from reduced convergence, although the anomalous inflow/outflow asymmetry still emerges. The analytic solutions suggest increased separation of slopes between the zero and residual evaporation results. The increased mismatch between the ana-

lytic and numerical results likely reflects the steady-state nature of the analytic solutions, greater sensitivity to the spatial details of the fields, and longer atmospheric adjustment.

5. Diagnostic interpretation of convective margin variability

The diagnostic discussed in this section, the precipitation variance budget, represents one that can be readily estimated from GCM outputs and is therefore a useful metric for model intercomparison. Approaches based on budgetary constraints have gained widespread use in studies of tropical precipitation: example applications include mechanistic analysis of the ENSO tropical teleconnection (Lintner and Chiang, 2005; Neelin and Su, 2005) and attribution of global warming impacts (Chou and Neelin, 2004). Many studies of land surface-atmosphere coupling have also employed budgetary analyses, especially the connection between evaporation and precipitation variances as inferred from soil moisture balance (Budyko, 1974; Brubaker et al., 1993; Koster et al., 2000, 2001; Wu et al., 2007). Here, we consider a budgetary decomposition of precipitation variance from the atmospheric side in order to highlight more explicitly the role of atmospheric processes in the generation of hotspots. Of course, while budgets can provide powerful insights into underlying mechanisms, it may be challenging to tease apart (direct) causal agents from (indirect) feedback processes, e.g., a large budget term does not imply causality. As will be seen, interpretation of the precipitation variance budget is not completely straightforward even for the idealized set-up considered here; however, viewing the budget in conjunction with margin variations proves instructive.

From the moisture equation (2), the precipitation variance budget is:

$$\begin{aligned} \sigma_P^2 = & \sigma_E^2 + \sigma_{-u_q \partial_x q}^2 + \sigma_{M_{qp} q \nabla \cdot \mathbf{v}}^2 + \\ & 2cov(E, -u_q \partial_x q) + 2cov(E, M_{qp} q \nabla \cdot \mathbf{v}) + \\ & 2cov(-u_q \partial_x q, M_{qp} q \nabla \cdot \mathbf{v}) \end{aligned} \quad (15)$$

Here, σ_A^2 denotes the variance of A , defined as $\sigma_A^2 = (N^2 - N)^{-1} \Sigma(A_i - \langle A \rangle)^2$, where $\langle A \rangle$ is the average of A . Similarly, $cov(A, B)$ denotes the covariance of A and B , $cov(A, B) = (N^2 - N)^{-1} \Sigma(A_i - \langle A \rangle)(B_i - \langle B \rangle)$. We emphasize that, for these simulations, the perturbation forcing is explicitly prescribed and is thus known *a priori*.

a. Moisture convergence and advection

Longitudinal profiles of the terms in (15) for the δ CTL and δ FIXED- β simulations (Figures 6a and 6b) demonstrate that the variance associated with moisture convergence, $\sigma_{M_{qp}q\nabla\cdot\mathbf{v}}^2$ (orange line), is typically the largest term. The dominance of moisture convergence is especially evident on the strongly-convecting side of the profile where $\sigma_{M_{qp}q\nabla\cdot\mathbf{v}}^2$ constitutes up to 90% of σ_P^2 (black line). On the other hand, the variance associated with horizontal moisture advection, $\sigma_{-u_q\partial_xq}^2$ (red line), contributes little to the total precipitation variance.

At first glance, the small variance contribution by horizontal moisture advection may appear counterintuitive: after all, it is through moisture advection that the perturbation forcing is applied. However, the apparent smallness of $\sigma_{-u_q\partial_xq}^2$ relative to σ_P^2 can be reconciled with the expectation that it should be larger by using the relationship (3) to expand the variance of moisture convergence:

$$\sigma_{M_{qp}q\nabla\cdot\mathbf{v}}^2 \approx \bar{\gamma}^2 \sigma_{R_{toa}}^2 + \bar{\gamma}^2 \sigma_{-u_q\partial_xq}^2 + 2\bar{\gamma}^2 \text{cov}(R_{toa}, -u_q\partial_xq) \quad (16)$$

where $\gamma = M_{qp}q/M$ (≈ 5). Although fluctuations in γ contribute to $\sigma_{M_{qp}q\nabla\cdot\mathbf{v}}^2$, their impact was observed to be sufficiently small to warrant their neglect in (16). The decomposition of moisture convergence reveals that $u_q\partial_xq$ is the dominant contribution to $\sigma_{M_{qp}q\nabla\cdot\mathbf{v}}^2$ (Figure 6c); thus, moisture advection does significantly contribute to σ_P^2 , albeit indirectly.

Like moisture convergence, moisture advection can be partitioned according to its definition, i.e.,

$$\sigma_{-u_q\partial_xq}^2 = (\partial_x\bar{q})^2 \sigma_{u_q}^2 + \bar{u}_q^2 \sigma_{\partial_xq}^2 + 2\bar{u}_q \partial_x\bar{q} \text{cov}(u_q, \partial_xq) + \mathcal{R}_{adv} \quad (17)$$

where \mathcal{R}_{adv} is a residual consisting of higher-order terms, $\mathcal{R}_{adv} = \Sigma[u'_q\partial_xq' - \langle u'_q\partial_xq' \rangle][2(\bar{u}_q\partial_xq' + \partial_xq'u'_q) + (u'_q\partial_xq' - \langle u'_q\partial_xq' \rangle)]$. The largest contribution to $\sigma_{-u_q\partial_xq}^2$ arises from $\bar{u}_q\sigma_{\partial_xq}^2$. That is, as the margin shifts under u_q variations, the steepest portion of the humidity profile (which occurs on the weakly-convecting side of the margin) is displaced, inducing large variations in q and its horizontal gradient.

b. Evaporation

Of all terms appearing in (15), the evaporation variance, σ_E^2 , manifests the largest difference between δ CTL and δ FIXED- β . In the absence of interactive soil moisture perturbations, the contribution of E to P variance is small everywhere. By contrast, for δ CTL, the evaporative contribution approaches and even slightly exceeds the contribution from moisture convergence at low mean P .

σ_E^2 can be decomposed through its definition:

$$\sigma_E^2 = \bar{E}_p^2 \sigma_\beta^2 + \bar{\beta}^2 \sigma_{E_p}^2 + 2\bar{\beta}\bar{E}_p \text{cov}(\beta, E_p) + \mathcal{R}_E \quad (18)$$

where \mathcal{R}_E is a residual defined analogously to \mathcal{R}_{adv} , $\mathcal{R}_E = \Sigma[\beta'E'_p - \langle \beta'E'_p \rangle][2(\bar{E}_p\beta' + \bar{\beta}E'_p) + (\beta'E'_p - \langle \beta'E'_p \rangle)]$. Averaging the terms in the expansion (18) over x -values close to the maximum of σ_E^2 reveals rather nontrivial behavior in δ CTL (Table 1): while $\bar{E}_p^2 \sigma_\beta^2$ is the largest term, it is largely balanced by the covariance between β and E_p . The negative covariation of β' and E'_p can be understood as follows. For an anomalously wet surface ($\beta' > 0$), surface temperature (T_s) decreases. The cooler surface is associated with a lowered saturation specific humidity, which yields negative E'_p , since $E_p \propto q_{surf}^{sat}(T_s) - q_{surf}$. For δ FIXED- β , on the other hand, only the variance associated with E_p is nonzero (since $\beta' = 0$), but the magnitude of this term ($0.2 \text{ mm}^2 \text{ day}^{-2}$) is considerably reduced relative to its value in δ CTL ($9.6 \text{ mm}^2 \text{ day}^{-2}$). This behavior illustrates a cautionary aspect of budgetary approaches, namely that they may obfuscate underlying physical mechanisms through covariances and compensation between terms.

The peak value of the ratio σ_E^2/σ_P^2 for δ CTL, 0.4, coincides with $P \approx 2 \text{ mm day}^{-1}$, consistent with localization of the strongest soil moisture-precipitation coupling between the most strongly convecting and nonconvecting conditions. (For $P < 2 \text{ mm day}^{-1}$, $\text{cov}(E, M_{qp}q\nabla\cdot\mathbf{v})$ dominates σ_P^2 .) Considering the variance differences between δ CTL and δ FIXED- β further highlights the importance of interactive soil moisture to precipitation variability (Figure 7a). Note that the variance differences have been plotted as functions of mean P , which in the idealized QTCM1 configuration is effectively a monotonic function of the distance from the edge of the convection zone. For $P < 4 \text{ mm day}^{-1}$, the difference in σ_E^2 ($\Delta\sigma_E^2$) accounts for all of the difference in σ_P^2 ($\Delta\sigma_P^2$) between the two simulations; in fact, since $\Delta\sigma_E^2 > \Delta\sigma_P^2$ for low mean P , the difference in the sum of remaining variance terms is negative. On the other hand, at high mean P , $\Delta\sigma_P^2$ is accounted for by the remaining terms, which include covariances with E .

One interpretation of the behavior in Figure 7a is that $\Delta\sigma_P^2 - \Delta\sigma_E^2$ represents a downstream, nonlocal feedback to soil moisture perturbations. In this view, a substantial portion of the precipitation change is only realized downstream of where the E contribution to P variance is maximized, i.e., at larger mean P values, where $\sigma_{M_{qp}q\nabla\cdot\mathbf{v}}^2$ dominates σ_P^2 . Thus, the P changes associated with interactive β occur over a larger range of mean P values (or, here, a larger spatial scale) than do the evaporative changes themselves. The nonlocality im-

plied by $\Delta\sigma_P^2 - \Delta\sigma_E^2$ is qualitatively consistent with the analysis of Schär et al., (1999), which stressed the role of horizontal advection (and nonlocality) to soil moisture-precipitation coupling.

c. Effect of changes to the convective parameterization

We also briefly comment on the effect of simulation physics—specifically, the convective parameterization—in determining the locality of the soil moisture-precipitation coupling. Convective parameterizations represent a significant source of divergence among current generation climate models, and a wide range of simulated quantities are known to be sensitive to the details of convective parameterizations (Zhang and McFarlane, 1995; Maloney and Hartmann, 2001; Gochis et al., 2002; Knutson and Tuleya, 2004). To illustrate how convective parameterizations can affect land surface-atmosphere coupling, we performed two additional sets of idealized QTCM1 simulations with lower and higher values of the convective adjustment timescale (τ_c) in the model’s Betts and Miller (1986) convection scheme. The principal impact of decreasing (increasing) τ_c is a steepening (flattening) of the mean edge of the convection zone. Decreasing τ_c further increases precipitation variability under u_q perturbations.

Alterations to τ_c have a demonstrable impact on the P and E variance differences (Figure 7b). Overall, the values of $\Delta\sigma_P^2$ and $\Delta\sigma_E^2$ increase as τ_c decreases. However, the contribution of $\Delta\sigma_E^2$ to $\Delta\sigma_P^2$ is seen to decrease as τ_c is reduced, while the peak of $\Delta\sigma_P^2$ is shifted deeper into the convection zone, i.e., toward higher mean P . These features suggest an increase of the downstream, nonlocal contributions to $\Delta\sigma_P^2$ as τ_c is reduced. A broader implication of such behavior is that the characteristics of land-atmosphere coupling in models—e.g., the degree of “hotspottedness” expressed by a model—can be impacted by parameters in the convection scheme.

6. Example of the soil moisture effect on precipitation seasonality

Over an annual cycle, the location of peak tropical convection varies latitudinally with changes in R_{toa} . Other factors may substantially modulate the latitude of peak convection. In the case of monsoon systems, for example, local land-ocean thermal contrasts may exert a leading-order influence on the intensity and duration of monsoonal rainfall (e.g., Steiner et al., 2008). Apart from the meridional seasonality of tropical precipitation, some zonal seasonality is also evident: for tropical South America, the eastern equatorial Amazon experiences its driest conditions during austral spring (Wang and Fu,

2002). Such seasonality is driven both by local land-ocean thermal contrasts and interactions of convection with large-scale circulation.

The inflow-evaporative moistening asymmetry described in Sections 3 and 4 may potentially contribute to land region seasonality, which we briefly explore here. We limit focus to the seasonal cycle of P at 5°S over the northeastern corner of South America as simulated by QTCM1 configured with realistic geometry, as in Section 2. The choice of region is motivated by the straightforward applicability of the LN07 prototype to the convective margin behavior here. Specifically, the circulation geometry is relatively simple, consisting of mostly zonal trade wind inflow from the equatorial Atlantic.

a. Impact of changing soil moisture holding capacity

In order to estimate soil moisture impacts on the convective margin at 5°S , we consider two experiments in which w_0 is set to either 150 mm or 15 mm. Varying w_0 corresponds to the alteration of one or more of the surface characteristics, such as vegetation type or fraction of bare soil, that affect the capacity of the surface to retain moisture. A value of 15 mm approximates a bare, “deforested” surface for which the soil moisture holding capacity is severely restricted. From the analysis in Section 3d, the characteristic decay timescale of the $w_0 = 15$ mm surface is of order 5 days.

The convective margin as simulated by QTCM1 for $w_0 = 150$ mm displays a pronounced seasonal cycle (Figure 8, black line). From January-July, the convective edge at 5°S lies near or to the east of the Atlantic coast. At the beginning of August, the margin recedes sharply westward, approaching roughly 50°W , or 1300 km from the Atlantic coastline, by the beginning of September. Thereafter, the margin advances eastward through the end of the year. To leading order, such seasonality is consistent with the seasonal evolution of tropical Atlantic SSTs, which are coolest when the margin is close to its maximum westward longitude. In the context of the LN07 prototype, the cool ocean surface is associated with low q_0 , which (for other factors being more-or-less equal) results in x_c occurring relatively far to the west of the Atlantic coast.

It is important to point out the occurrence of some significant small scale structure in the observed precipitation field, such as the intense rainfall band along the Atlantic coast, that do not appear in the QTCM1 simulations analyzed here. As discussed in Kousky (1980), this coastal rainfall maximum is associated with diurnally-varying land-sea breeze circulations, the physics of which are not represented in the QTCM1 framework. Additional smaller-scale structure associated with topo-

graphic forcing and mesoscale circulations is also absent at the resolution of the QTCM1 simulations.

The net impact of reducing w_0 induces a westward shift of the margin of up to 2° relative to the simulation with larger w_0 . As the margin recedes westward from the land-ocean interface, the nonconvecting land surface between the Atlantic and the margin begins to dry. The low w_0 surface loses moisture rapidly once the westward margin displacement begins. Thus, the low-level inflow into the convection zone is relatively drier, so the inflowing air masses must experience further vertical convergence-induced moistening to achieve the same $q_c(T)$, resulting in lengthening the distance to reach the margin.

b. Explicit removal of residual soil moisture outside of the convection zone

To this point, we have not distinguished between the effect of soil moisture anomalies outside of the convection zone (i.e., between the Atlantic coast and x_c^E) relative to those within the convection zone. While the inflow-evaporation interaction described above only requires nonconvecting region soil moisture, the presence of soil moisture within the convection zone could potentially affect margin behavior. For example, local evaporative recycling increases precipitation, which in turn induces cloud-radiative effects that may alter the temperature profile in the vicinity of the margin, thus affecting $q_c(T)$. To demonstrate more conclusively that it is the soil moisture outside of the convection zone that matters most here, we performed an additional simulation, this time explicitly removing the soil moisture from nonconvecting region region after the margin has retreated. Figure 9 shows cross-sections of precipitation, evaporation, and soil wetness at 5°S for this simulation as well as the standard set-up (in gray and black, respectively), averaged over pentads 50-54. Comparison of the two precipitation profiles reveals a pronounced longitudinal margin displacement, by $2\text{-}3^\circ$, which substantiates the role of nonconvecting region moisture in producing the margin shift.

7. Summary and conclusions

Straightforward extension of the LN07 convective margins prototype to include the effects of soil moisture acting through evaporation provides some basic intuition about how land surface conditions modulate the transition from nonconvecting to convecting conditions over tropical continents. For the case of low-level oceanic inflow into a land region convection zone, the integrated effect of evaporation along the inflow trajectory moistens

air masses approaching the margin; relative to a comparable trajectory over a dry surface, the moisture tends to increase more rapidly along the inflow path, as expected. Given a fixed convective threshold, the integrated evaporation effect induces a shift of the convective margin toward the inflow point. This shift depends on E as well as factors determining the large-scale convergence along the trajectory, notably the top-of-the-atmosphere radiative heating R_{toa} . In fact, nonzero E along the inflow trajectory lowers the large-scale convergence, but for realistic parameters, the direct evaporative moistening dominates over the convergence reduction.

The analytic prototype further demonstrates how land surface evaporation affects margin variability. In particular, it was shown that the inclusion of E yields an asymmetry in the margin displacements to low-level wind perturbations: under anomalous inflow conditions, marginal displacements are smaller than those for anomalous outflow conditions of the same magnitude. That is, for anomalous low-level inflow, the margin moves over a residually wet surface, which moistens the inflow into the convecting region, thereby allowing $q_c(T)$ to be met earlier along the inflow path. Idealized experiments with an intermediate level complexity model, QTCM1, subject to imposed high-frequency inflow wind perturbations confirmed the presence of this asymmetry; on the other hand, under suppression of nonconvecting region soil moisture, the asymmetry did not occur. On seasonal timescales, it was noted that the inflow-evaporative moistening mechanism may be of relevance to the timing and spatial extent of marginal advances and retreats.

Within QTCM1, behavior reminiscent of the hotspots of strong soil moisture-convective coupling seen in previous studies such as (e.g., Koster et al., 2004) was also observed. Comparison of simulations with and without interactive soil moisture suggested amplification of precipitation variability via soil moisture by $\sim 20\%$ in the vicinity of the convective margin. Despite the idealized nature of the simulations in which hotspot behavior was observed, analysis of precipitation variance budgets for these simulations proved challenging, because of the multiple terms involved, although the mechanistic understanding provided by the margins framework was useful for interpreting some features of the budget. One aspect of particular note is the nonlocality of soil moisture impacts, with a significant portion of the precipitation response realized downstream of where soil moisture and evaporation are most variable.

Alteration of the model's convection scheme, specifically the timescale for convective adjustment, further demonstrates how the characteristics of hotspots may be affected by model representation of atmospheric processes. Other "atmospheric-side" factors that may af-

fect hotspot characteristics, as seen in the prototype, include top-of-the-atmosphere heating and large-scale convergence; the mean and variance of inflow wind; and the convective moisture threshold. These factors interact nonlinearly in setting the convective margin, and they may generate substantial regional variation in margin sensitivity to perturbations. Together, they provide an indication of why the strength of simulated land-atmosphere coupling may vary among models.

Acknowledgments. The authors thank R. D. Koster, N. Zeng, P. L. Silva Dias, M. Notaro, and an anonymous reviewer for discussion and comments and J. E. Meyerson for graphical assistance. This work was supported partly by National Oceanic and Atmospheric Administration NA08OAR4310882 and NA08OAR4310597 and National Science Foundation ATM-0645200. JDN acknowledges sabbatical support from the J. S. Guggenheim Memorial Foundation.

REFERENCES

- Atlas, R., N. Wolfson, and J. Terry, 1993: The effect of SST and soil-moisture anomalies on GLA model simulations of the 1988 U.S. summer drought. *J. Climate*, **6**, 2034–2048.
- Barnston, A.G., and P.T. Schickedanz, 1984: The effect of irrigation on warm season precipitation in the southern Great Plains. *J. Clim. Appl. Meteor.*, **23**, 865–888.
- Beljaars, A.C.M., P. Viterbo, M.J. Miller, and A.K. Betts, 1996: The anomalous rainfall over the United States during July, 1993: Sensitivity to land surface parameterization and soil moisture anomalies. *Mon. Wea. Rev.*, **124**, 362–383.
- Betts, A. K., and M. J. Miller, 1986: A new convective adjustment scheme. 2. Single column model tests using GATE Wave, BOMEX, ATEX, and arctic air-mass data sets. *Quart. J. Roy. Meteor. Soc.*, **112**, 693–709.
- Brubaker, K.L., D. Entekhabi, and P.S. Eagleson, 1993: Estimation of continental precipitation recycling. *J. Climate*, **6**, 1077–1089.
- Budyko, M.I., 1974: *Climate and Life*, 508 pp., Academic Press, New York.
- Charney, J. G., 1975: Dynamics of deserts and drought in the Sahel. *Quart. J. Roy. Meteor. Soc.*, **101**, 193–202.
- Chou, C., and J.D. Neelin, 2003: Mechanisms limiting the northward extent of the northern summer monsoons over North America, Asia, and Africa. *J. Climate*, **16**, 406–425.
- Chou, C., and J.D. Neelin, 2004: Mechanisms of global warming impacts on regional tropical precipitation. *J. Climate*, **17**, 2688–2701.
- Chou, C., J.D. Neelin, C.-A. Chen, and J.-Y. Tu, 2008: Evaluating the “rich-get-richer” mechanism in tropical precipitation change under global warming. *J. Climate*, **in press**.
- Delire, C., J. A. Foley, and S. Thompson, 2004: Long-term variability in a coupled atmosphere-biosphere model. *J. Climate*, **17**, 3947–3959.
- Delworth, T.L., and S. Manabe, 1988: The influence of potential evaporation on the variabilities of simulated soil wetness and climate. *J. Climate*, **1**, 523–547.
- Dirmeyer, P.A., R.D. Koster, and Z.C. Guo, 2006: Do global models properly represent the feedback between land and atmosphere? *J. Hydrometeorol.*, **7** (6), 1177–1198.
- D’Odorico, P., and A. Porporato, 2004: Preferential states in soil moisture and climate dynamics. *Proc. Nat. Acad. Sci.* **101** (24), 8848–8851.
- Douville H., F. Chauvin, S. Planton, J.F. Royer, D. Salas-Melia, S. Tyteca, 2002: Sensitivity of the hydrological cycle to increasing amounts of greenhouse gases and aerosols. *Clim. Dyn.*, **20**, 45–68.
- Douville, H., 2003: Assessing the influence of soil moisture on seasonal climate variability in AGCMs. *J. Hydrometeorol.*, **4** (6), 1044–1066.
- Entekhabi, D., I. Rodríguez-Iturbe, and F. Castelli, 1996: Mutual interaction of soil moisture state and atmospheric processes. *J. Hydrology*, **184**, 3–17.
- Findell, K.L., and E.A.B. Eltahir, 1997: An analysis of the soil moisture-rainfall feedback based on direct observations from Illinois. *Water Resources Res.*, **33**, 725–735.
- Findell, K.L., and E.A.B. Eltahir, 1999: Analysis of the pathways relating soil moisture and subsequent rainfall in Illinois. *J. Geophys. Res.- Atmos.*, **104**, 31565–31574.
- Gochis, D.J., W.J.A. Shuttleworth, and Z.L. Yang, 2002: Sensitivity of the modeled North American monsoon regional climate to convective parameterization. *Mon. Wea. Rev.*, **130**, 1282–1298.
- Guo, Z., and the GLACE Team, 2006: GLACE: The Global Land-Atmosphere Coupling Experiment. 2. Analysis., *J. Hydrometeorol.*, **7**, 611–625.
- Hong, S.-Y., and E. Kalnay, 2000: Role of sea surface temperature and soil-moisture feedback in the 1998 Oklahoma-Texas drought. *Nature*, **408**, doi:10.1038.35048548, 842–844.
- IPCC, 2007: Climate Change 2007: The Physical Science Basis. Contribution of Working Group I to the Fourth Assessment Report of the Intergovernmental Panel on Climate Change. Solomon, S., D. Qin, M. Manning (eds.).
- Johns, T.C., J.M. Gregory, W.J. Ingram, C.E. Johnson, A. Jones, J.A. Lowe, J.F.B. Mitchell, D.L. Roberts, D.M.H. Sexton, D.S. Stevenson, S.F.B. Tett, and M.J. Woodage, 2003: Anthropogenic climate change for 1860 to 2100 simulated with the HadCM3 model under updated emissions scenarios. *Clim. Dyn.*, **20**, 583–612.
- Knutson, T.R., and R.E. Tuleya, 2004: Impact of CO₂-induced warming on simulated hurricane intensity and precipitation: Sensitivity to the choice of climate model and convective parameterization. *J. Climate*, **17**, 3477–3495.
- Koster, R.D., M.J. Suarez, and M. Heiser, 2000: Variance and predictability of precipitation at seasonal-to-interannual timescales. *J. Hydrometeorol.*, **1**, 26–46.
- Koster, R.D., P.A. Dirmeyer, P.C.D. Milly, and G.L. Russell, 2001: Comparing GCM-generated land surface water budgets using a simple common framework. In *Land Surface Hydrology, Meteorology, and Climate: Observations and Modeling*, V. Lakshmi, J. Albertson, and J. Schaake, Editors, American Geophysical Union, Washington, D.C., 95–105.
- Koster, R.D., P.A. Dirmeyer, A.N. Hahmann, R. Ijpeelaar, L. Tyahla, P. Cox, and M.J. Suarez, 2002: Comparing the degree of land-atmosphere interaction in four atmospheric general circulation models. *J. Hydrometeorol.*, **3**, 363–375.
- Koster, R.D., M.J. Suarez, R.W. Higgins, and H.M. Van den Dool, 2003: Observational evidence that soil moisture variations affect precipitation. *Geophys. Res. Lett.*, **30**, doi:10.1029/2002GL016571.
- Koster, R.D., and the GLACE Team, 2004: Regions of strong coupling between soil moisture and precipitation. *Science*, **305**, 1138–1140.
- Koster, R.D., and M.J. Suarez, 2004: Suggestions in the observational record of land-atmosphere feedback operating at seasonal time scales. *J. Hydrometeorol.*, **5**, 567–572.
- Kousky, V.E., 1980: Diurnal rainfall variation in Northeast Brazil. *Mon. Wea. Rev.*, **108**, 488–498.
- Lin, J.W.-B., J.D. Neelin, and N. Zeng, 2000: Maintenance of tropical intraseasonal variability: Impact of evaporation-wind feedback and midlatitude storms. *J. Atmos. Sci.*, **57**, 2793–2823.
- Lintner, B.R., and J.C.H. Chiang, 2005: Reorganization of tropical climate during El Niño: a weak temperature gradient approach. *J. Climate*, **18** (24), doi:10.1175/JCLI3580.1, 5312–5329.
- Lintner, B.R., and J.D. Neelin, 2007: A prototype for convective margin shifts. *Geophys. Res. Lett.*, **34** (5), doi:10.1029/2006GL027305, L05812.
- Maloney, E.D., and D.L. Hartmann, 2001: The sensitivity of intraseasonal variability in the NCAR CCM3 to changes in convective parameterization. *J. Climate*, **14**, 2015–2034.
- Moore, N., and S. Rojstaczer, 2002: Irrigation’s influence on precipitation: Texas High Plains, USA. *Geophys. Res. Lett.*, **29**, Art. No. 1755.
- Neelin, J.D., and N. Zeng, 2000: A quasi-equilibrium tropical circulation model—formulation. *J. Atmos. Sci.*, **57**, 1741–1766.
- Neelin, J.D., and H. Su, 2005: Moist teleconnection mechanisms for the tropical South American and Atlantic sector. *J. Climate*, **18**, 3928–3950.
- Neelin, J.D., M. Munnich, H. Su, J.E. Meyerson, and C.E. Holloway, 2006: Tropical drying trends in global warming models and observations. *Proc. Nat. Acad. Sci.*, **103**, 6110–6115.
- Notaro, M., Z. Liu, and J. W. Williams, 2006: Observed vegetation-climate feedbacks in the United States. *J. Climate*, **19**, 763–786.
- Notaro, M., 2008: Statistical identification of global hot spots in soil moisture feedbacks among IPCC AR4 models. *J. Geophys. Res.*, **113**, D09101.
- Pal, J.S., and E.A.B. Eltahir, 2001: Pathways relating soil moisture conditions to future summer rainfall within a model of the land-atmosphere system. *J. Climate*, **14**, 1227–1242.
- Pal, J.S., and E.A.B. Eltahir, 2003: A feedback mechanism between soil-moisture distribution and storm tracks. *Quart. J. Roy. Meteor. Soc.*, **129**, 2279–2297 Part A.
- Schär, C., D. Luthi, and U. Beyerle, 1999: The soil-precipitation feedback: A process study with a regional climate model. *J. Climate*, **12**, 729–741.
- Shukla, J., and Y. Mintz, 1982: The influence of land-surface evapotranspiration on Earth’s climate. *Science*, **215**, 1498–1501.
- Sobel, A.H., and C.S. Bretherton, 2000: Modeling tropical precipitation in a single column. *J. Climate*, **13**, 4378–4392.
- Soden, B.J., and I.M. Held, 2006: Robust responses of the hydrological cycle to global warming. *J. Climate*, **19**, 5686–5699.
- Steiner, A.L., J.S. Pal, S.A. Rauscher, J.L. Bell, N.S. Diffenbaugh, L.C. Sloan, and F. Giorgi, 2008: Land surface coupling in regional climate simulations of the West African monsoon. *Clim Dyn.* **in preparation**.

- Su, H., J.D. Neelin, and J.E. Meyerson, 2003: Sensitivity of tropical tropospheric temperature to sea surface temperature forcing. *J. Climate*, **16**, 1283–1301.
- Stidd, C.K., 1975: Irrigation increases rainfall? *Science*, **188**, 279–281.
- Taylor, C.M., F. Said, and T. Lebel, 1997: Interactions between the land surface and mesoscale rainfall variability during HAPEX-Sahel. *Mon. Wea. Rev.*, **125**, 2211–2227.
- Taylor, C.M., and T. Lebel, 1998: Observational evidence of persistent convective-scale rainfall patterns. *Mon. Wea. Rev.*, **126**, 1597–1607.
- Taylor, C.M., R.J. Ellis, D.J. Parker, R.R. Burton, and C.D. Thorncraft, 2003: Linking boundary layer variability with convection: A case-study from JET2000. *Quart. J. Roy. Meteor. Soc.*, **129**, 2233–2253.
- Vinnikov, K.Y., A. Robock, N.A. Speranskaya, and C.A. Schlosser, 1996: Scales of temporal and spatial variability of soil moisture. *J. Geophys. Res.*, **101**, 7163–7174.
- Wang, H., and R. Fu, 2002: Cross-equatorial flow and seasonal cycle of precipitation over South America. *J. Climate*, **15**, 1591–1608.
- Williams, K.D., C.A. Senior, and J.F.B. Mitchell, 2001: Transient climate change in the Hadley Centre models: The role of physical processes. *J. Climate*, **14**, 2659–2674.
- Wu, W., R.E. Dickinson, H. Wang, Y. Liu, and M. Shaikh, 2007: Covariabilities of spring soil moisture and summertime United States precipitation in a climate simulation. *Int. J. Climatol.*, **27**, 429–438.
- Xie, P.P., and P.A. Arkin, 1997: Global precipitation: A 17-year monthly analysis based on gauge observations, satellite observations, and numerical model output. *Bull. Amer. Meteor. Soc.*, **78**, 2539–2558.
- Xue, Y., and J. Shukla, 1993: The influence of land-surface properties on Sahel climate. Part 1: Desertification. *J. Climate*, **6**, 2232–2245.
- Yu, J.-Y., C. Chou, and J. D. Neelin, 1998: Estimating the gross moist stability of the tropical atmosphere. *J. Atmos. Sci.*, **55**, 1354–1372.
- Zeng, N., J.D. Neelin, K.M. Lau, and C.J. Tucker, 1999: Enhancement of interdecadal climate variability in the Sahel by vegetation interaction. *Science*, **286**, 1537–1540.
- Zeng, N., J.D. Neelin, and C. Chou, 2000: A quasi-equilibrium tropical circulation model—Implementation and simulation. *J. Atmos. Sci.*, **57**, 1767–1796.
- Zhang, G.J., and N.A. McFarlane, 1995: Sensitivity of climate simulations to the parameterization of cumulus convection in the Canadian Climate Center general-circulation model. *Atmos.-Ocean*, **33**, 407–446.
- Zheng, X., and E.A.B. Eltahir, 1998: A soil moisture-rainfall feedback mechanism. 2. Experiments with a simple numerical model. *Water Resource Res.*, **34**, 777–785.

Table and Figure Captions

TABLE 1: Breakdown of σ_E^2 for the δ CTL and δ FIXED- β simulations. Values tabulated are in units of $\text{mm}^2 \text{day}^{-2}$.

FIGURE 1: (a) 3-month seasonal mean precipitation standard deviations of the QTCM1 CTL and (b) ratio of CTL to FIXED- β simulations. The shaded contours in (a) are in units of mm day^{-1} , while those in (b) are nondimensional. In (b), only those regions where the ratio exceeds 1 are shaded. Line contours denote seasonal mean precipitation (in mm day^{-1}).

FIGURE 2: Convective margin prototype schematic. Shown are the geometry of the prototype, which is oriented to reflect the land-ocean configuration for Northeastern South America, and the principal elements included in it (see text). The solid blue and black lines are precipitation and moisture profiles over the land region. The dashed lines reflect behavior in the presence of transients that tend to smear the edge of the convection zone (see LN07). In later discussion, anomalous inflow (outflow) conditions correspond to stronger (weaker) low-level flow in the direction of the horizontal gray arrow.

FIGURE 3: (a) Dependence of x_c^E (equation 11) on top-of-the-atmosphere radiation (R_{toa}) for different values of evaporation (E). The curves plotted (in units of 1000 km relative to the inflow point) correspond to $E = 0, 10, \text{ and } 20 \text{ W m}^{-2}$ (red, green, and blue respectively). Note that a value of u_q of 1 m s^{-1} has been assumed. Dashed vertical lines correspond to asymptotes of x_c^E , which occur at $R_{toa} = -M_{qp}q_c(T)M_s^{-1}E$. (b) Logarithmic derivative of x_c^E with respect to E for R_{toa} of 10, 30, 50, and 70 W m^{-2} (black, red, green, and blue, respectively). Values given are in units of percent per (W m^{-2}).

FIGURE 4: Time-mean precipitation profiles (solid lines) as simulated by the idealized ‘‘tropical strip’’ configuration of QTCM1 (see text in Section 4a for a detailed description): δ CTL (red); δ FIXED- β (blue); δ NOWETMEM (green). The dashed lines are standard deviations of for each case. The distance along the horizontal axis has been normalized by the x_c obtained in the absence of perturbation forcing, with a value of 0 denoting the land-ocean interface and a value of 1 denoting the location of the nonperturbed margin.

FIGURE 5: Relationships of convective margin locations x_c^E to applied windfield perturbations δu_0 using the QTCM1 tropical strip configuration for (a) $R_{toa} \approx 70 \text{ W m}^{-2}$ and (b) $R_{toa} \approx 26 \text{ W m}^{-2}$. The data points shown consist of bin-averages according to δu_0 values with bin widths defined by percentiles of the normal distribution for δ CTL (red), δ FIXED- β (blue), and δ NOWETMEM (green). The x_c^E values represent the margin location on the final day of each 10-day interval

of perturbation, normalized by the location of the non-perturbed margin. Error bars correspond to the standard error, $se_i = \sigma_i/\sqrt{N_i}$, of each bin, where σ_i is the standard deviation of each bin average and N_i is the number of data points per bin. Also shown in each panel are the steady-state analytic solutions estimated from equations (13) (no evaporation; black lines) and (15) (residual evaporation; gray lines).

FIGURE 6: Precipitation variance budgets for (a) δ CTL and (b) δ FIXED- β . Shown are the variances of precipitation (black), component variances associated with moisture convergence (orange), moisture advection (red), and evaporation (green), and covariances of moisture convergence-moisture advection (dark blue), moisture convergence-evaporation (light blue), and moisture advection-evaporation (purple). Note the x-axis is normalized as in Figure 4. Panel (c) illustrates the decomposition of $\sigma_{M_{qp}q\nabla \cdot v}^2$ (black) into variances associated with R_{toa} (green) and $u_q\partial_x q$ (red) and the covariance of $R_{toa}-u_q\partial_x q$ (blue) for δ CTL (solid lines) and δ FIXED- β (dashed lines).

FIGURE 7: (a) Variance differences between δ CTL and δ FIXED- β . Shown are differences of σ_P^2 ($\Delta\sigma_P^2$; black) and σ_E^2 ($\Delta\sigma_E^2$; gray), in units of $\text{mm}^2 \text{day}^{-2}$, plotted against the mean P (in mm day^{-1}). Also shown is $\Delta\sigma_\beta^2$ (dashed line; relative to the dimensionless axis on the right-hand side). (b), $\Delta\sigma_P^2$ (black) and $\Delta\sigma_E^2$ (gray) for $\tau_c = 0.5 \text{ hrs}$ (squares) and $\tau_c = 5 \text{ hrs}$ (triangles).

FIGURE 8: Zonal location of the convective margin over Northeastern South America at 5°S for 5-day (pentadal) averages. The black (gray) line illustrates the location of the 2 mm day^{-1} precipitation contour for a soil moisture holding capacity of 150 (15) mm. (Note that the range of pentads shown covers late May through December.) For comparison, the location of the 2 mm day^{-1} precipitation contour estimated from the CMAP precipitation data (squares, for 1979-2002) is also included. The shaded contours illustrate positive values of soil wetness difference of the 150 mm and 15 mm simulations.

FIGURE 9: Zonal cross-sections of precipitation (solid lines), evaporation (dashed lines), and soil wetness (squares) for the standard full geometry QTCM1 simulation (black) and the sensitivity simulation with soil moisture explicitly removed where $P = 0$ (gray). Results shown are averaged over pentads 50-54. The dashed vertical lines and light brown arrow indicate the region for which soil moisture is zeroed out in this averaging period. The dark brown shading highlights that the precipitation field is altered downstream of where the soil moisture is perturbed.

Term	δ CTL	δ FIXED- β
$\overline{E_p}^2 \sigma_\beta^2$	26.9	0
$\overline{\beta}^2 \sigma_{E_p}^2$	9.6	0.2
$2\overline{\beta E_p} cov(\beta, E_p)$	-23.1	0
\mathcal{R}_{Evap}	-8.9	0

TABLE 1: Breakdown of σ_E^2 for the δ CTL and δ FIXED- β simulations. Values tabulated are in units of $\text{mm}^2 \text{day}^{-2}$.

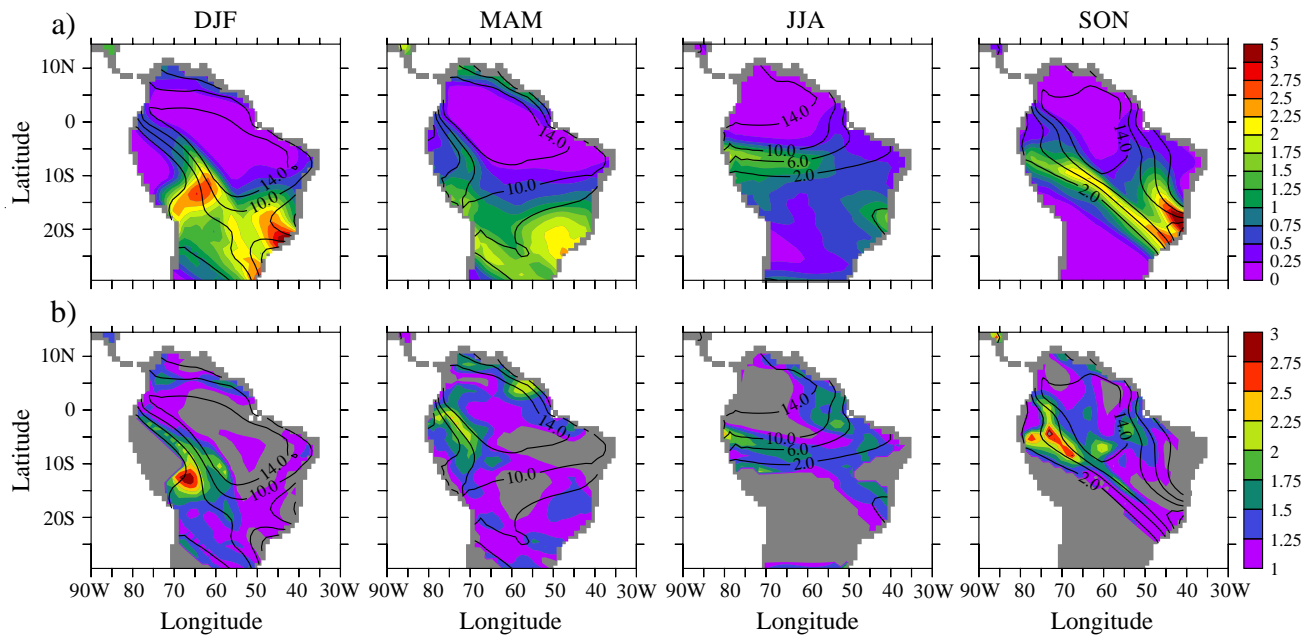


FIGURE 1: (a) 3-month seasonal mean precipitation standard deviations of the QTCM1 CTL and (b) ratio of CTL to FIXED- β simulations. The shaded contours in (a) are in units of mm day^{-1} , while those in (b) are nondimensional. In (b), only those regions where the ratio exceeds 1 are shaded. Line contours denote seasonal mean precipitation (in mm day^{-1}).

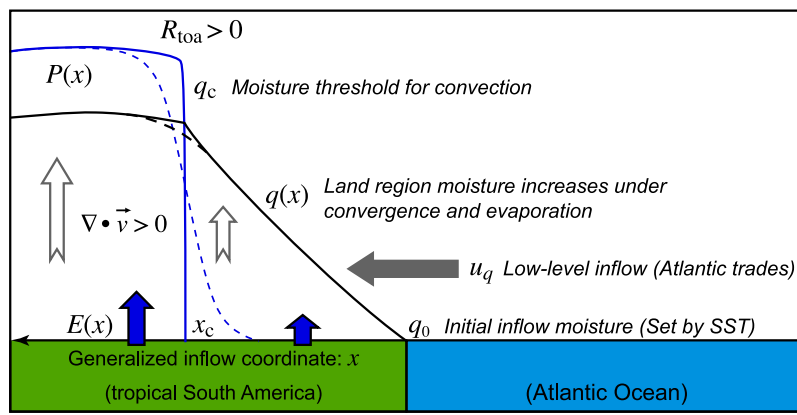


FIGURE 2: Convective margin prototype schematic. Shown are the geometry of the prototype, which is oriented to reflect the land-ocean configuration for Northeastern South America, and the principal elements included in it (see text). The solid blue and black lines are precipitation and moisture profiles over the land region. The dashed lines reflect behavior in the presence of transients that tend to smear the edge of the convection zone (see LN07). In later discussion, anomalous inflow (outflow) conditions correspond to stronger (weaker) low-low level flow in the direction of the horizontal gray arrow.

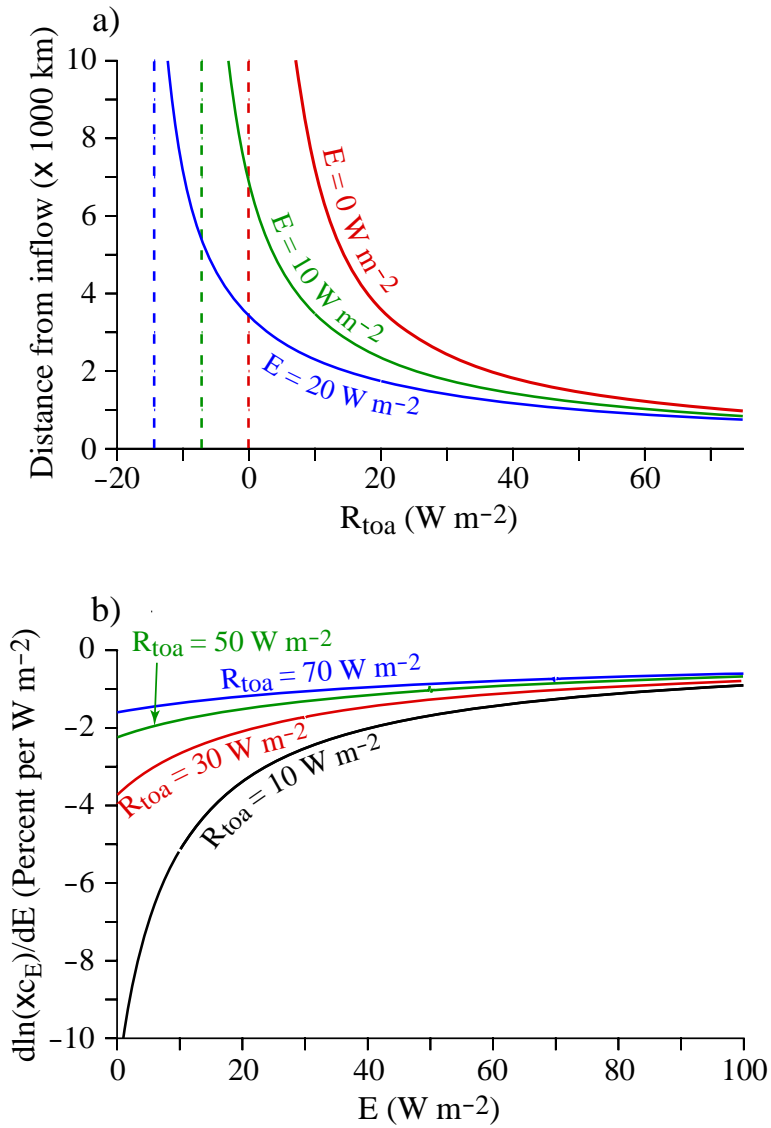


FIGURE 3: (a) Dependence of x_c^E (equation 11) on top-of-the-atmosphere radiation (R_{toa}) for different values of evaporation (E). The curves plotted (in units of 1000 km relative to the inflow point) correspond to $E = 0, 10,$ and 20 W m^{-2} (red, green, and blue respectively). Note that a value of u_q of 1 m s^{-1} has been assumed. Dashed vertical lines correspond to asymptotes of x_c^E , which occur at $R_{toa} = -M_{qp}q_c(T)M_s^{-1}E$. (b) Logarithmic derivative of x_c^E with respect to E for R_{toa} of 10, 30, 50, and 70 W m^{-2} (black, red, green, and blue, respectively). Values given are in units of percent per (W m^{-2}).

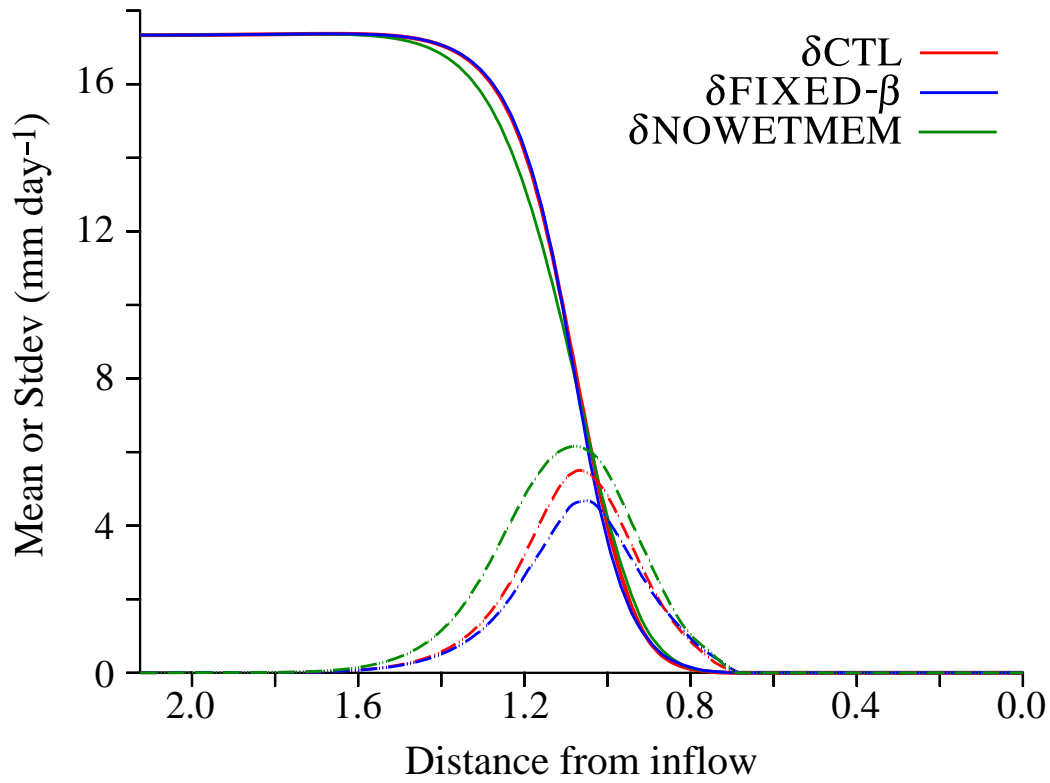


FIGURE 4: Time-mean precipitation profiles (solid lines) as simulated by the idealized “tropical strip” configuration of QTCM1 (see text in Section 4a for a detailed description): δ CTL (red); δ FIXED- β (blue); δ NOWETMEM (green). The dashed lines are standard deviations of for each case. The distance along the horizontal axis has been normalized by the x_c obtained in the absence of perturbation forcing, with a value of 0 denoting the land-ocean interface and a value of 1 denoting the location of the nonperturbed margin.

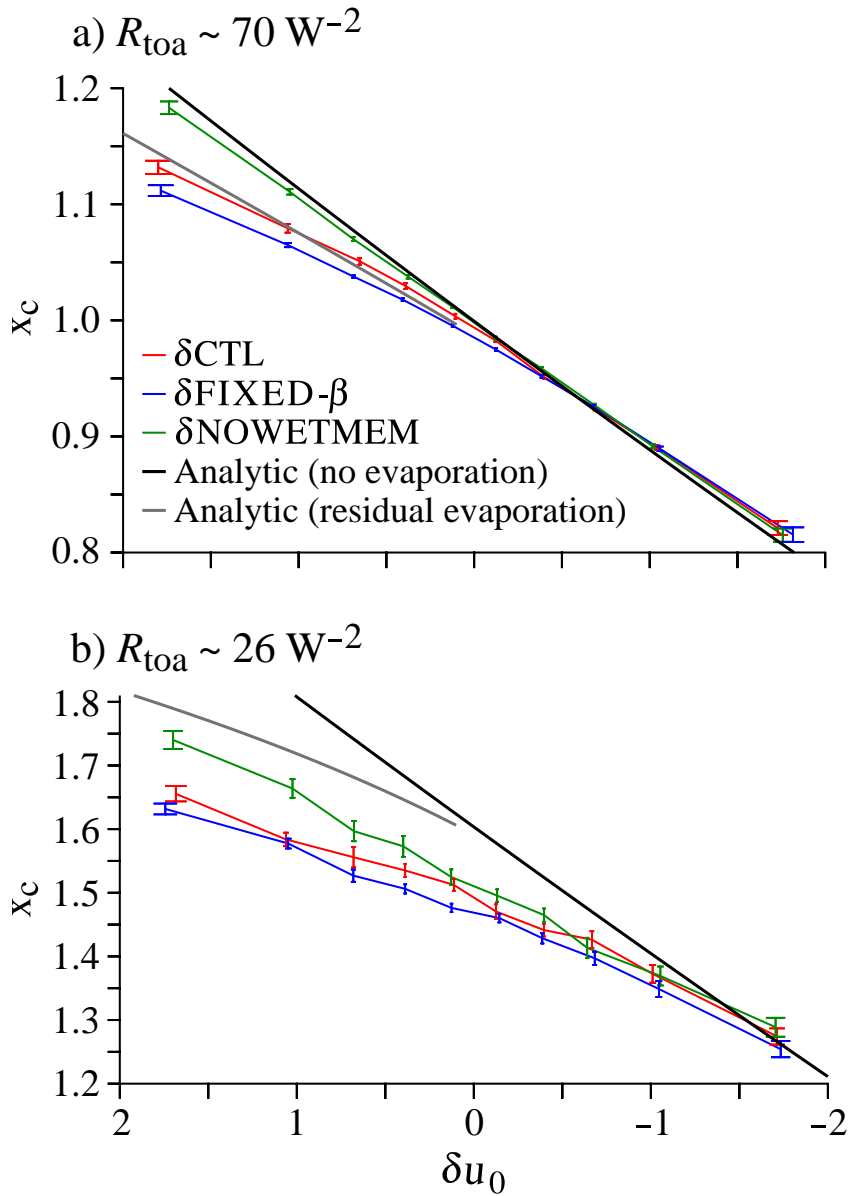


FIGURE 5: Relationships of convective margin locations x_c^E to applied windfield perturbations δu_0 using the QTCM1 tropical strip configuration for (a) $R_{\text{toa}} \approx 70 \text{ W m}^{-2}$ and (b) $R_{\text{toa}} \approx 26 \text{ W m}^{-2}$. The data points shown consist of bin-averages according to δu_0 values with bin widths defined by percentiles of the normal distribution for δCTL (red), $\delta\text{FIXED-}\beta$ (blue), and $\delta\text{NOWETMEM}$ (green). The x_c^E values represent the margin location on the final day of each 10-day interval of perturbation, normalized by the location of the nonperturbed margin. Error bars correspond to the standard error, $se_i = \sigma_i / \sqrt{N_i}$, of each bin, where σ_i is the standard deviation of each bin average and N_i is the number of data points per bin. Also shown in each panel are the steady-state analytic solutions estimated from equations (13) (no evaporation; black lines) and (15) (residual evaporation; gray lines).

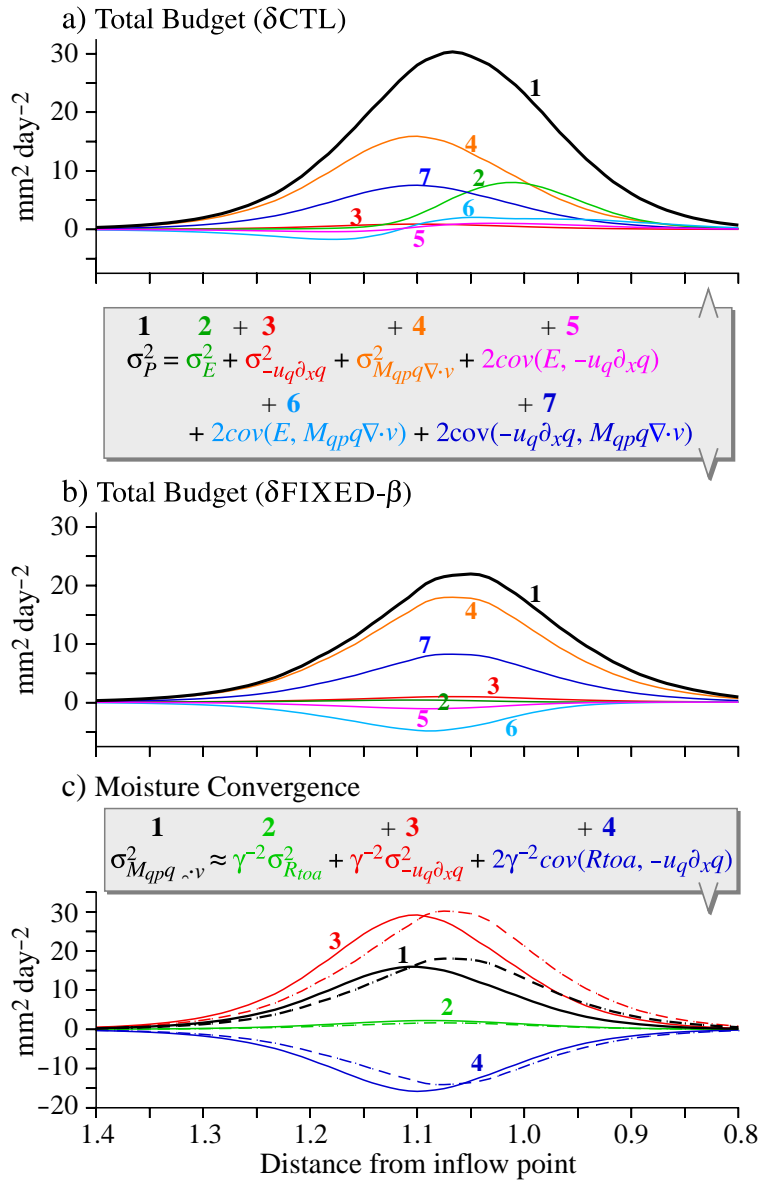


FIGURE 6: Precipitation variance budgets for (a) δCTL and (b) $\delta\text{FIXED-}\beta$. Shown are the variances of precipitation (black), component variances associated with moisture convergence (orange), moisture advection (red), and evaporation (green), and covariances of moisture convergence-moisture advection (dark blue), moisture convergence-evaporation (light blue), and moisture advection-evaporation (purple). Note the x-axis is normalized as in Figure 4. Panel (c) illustrates the decomposition of $\sigma_{M_{qpq} \nabla \cdot v}^2$ (black) into variances associated with R_{toa} (green) and $u_q \partial_x q$ (red) and the covariance of $R_{toa} - u_q \partial_x q$ (blue) for δCTL (solid lines) and $\delta\text{FIXED-}\beta$ (dashed lines).

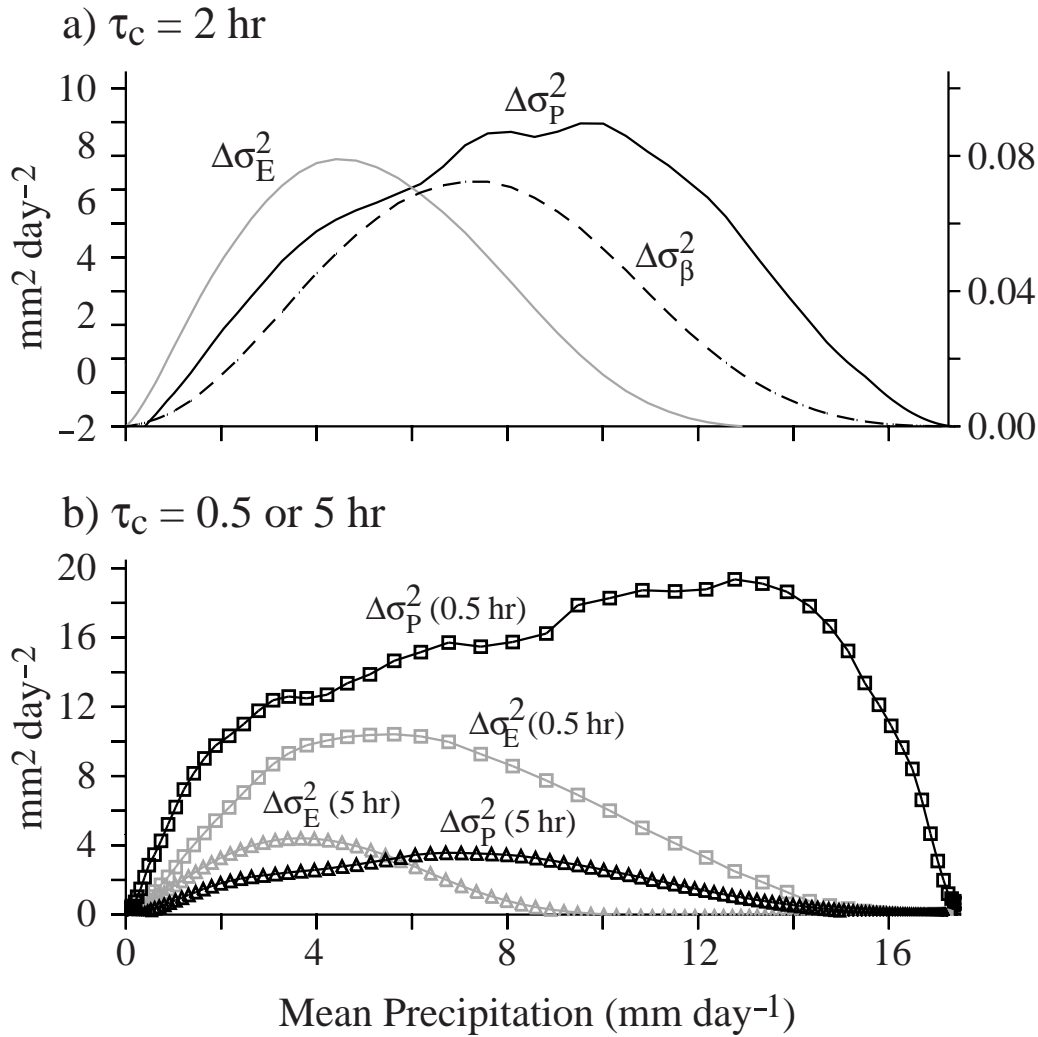


FIGURE 7: (a) Variance differences between δCTL and $\delta\text{FIXED-}\beta$. Shown are differences of σ_P^2 ($\Delta\sigma_P^2$; black) and σ_E^2 ($\Delta\sigma_E^2$; gray), in units of mm² day⁻², plotted against the mean P (in mm day⁻¹). Also shown is $\Delta\sigma_\beta^2$ (dashed line; relative to the dimensionless axis on the right-hand side). (b), $\Delta\sigma_P^2$ (black) and $\Delta\sigma_E^2$ (gray) for $\tau_c = 0.5$ hrs (squares) and $\tau_c = 5$ hrs (triangles).

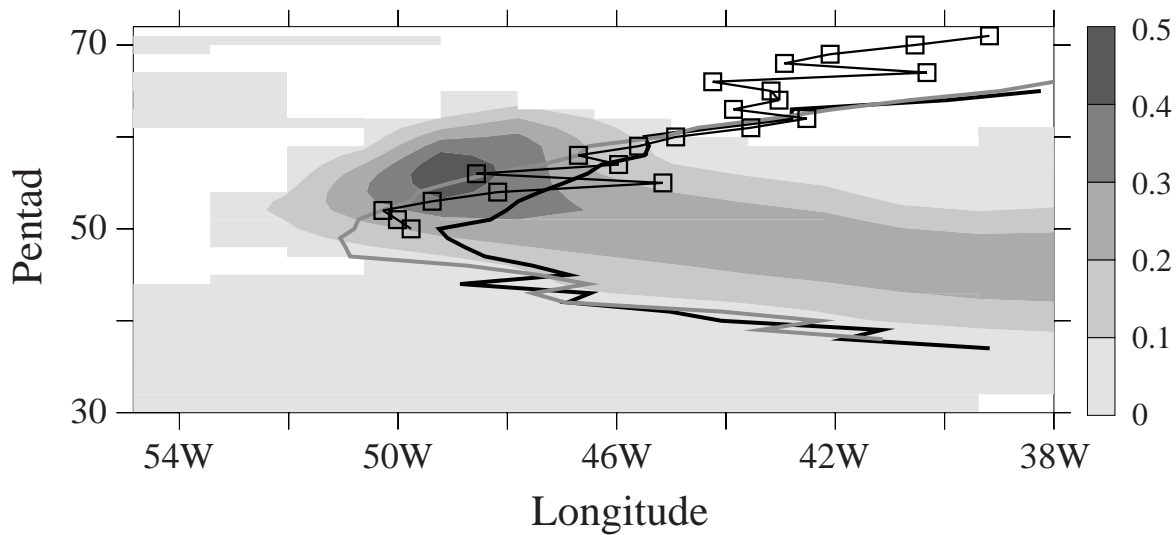


FIGURE 8: Zonal location of the convective margin over Northeastern South America at 5°S for 5-day (pentadal) averages. The black (gray) line illustrates the location of the 2 mm day⁻¹ precipitation contour for a soil moisture holding capacity of 150 (15) mm. (Note that the range of pentads shown covers late May through December.) For comparison, the location of the 2 mm day⁻¹ precipitation contour estimated from the CMAP precipitation data (squares, for 1979-2002) is also included. The shaded contours illustrate positive values of soil wetness difference of the 150 mm and 15 mm simulations.

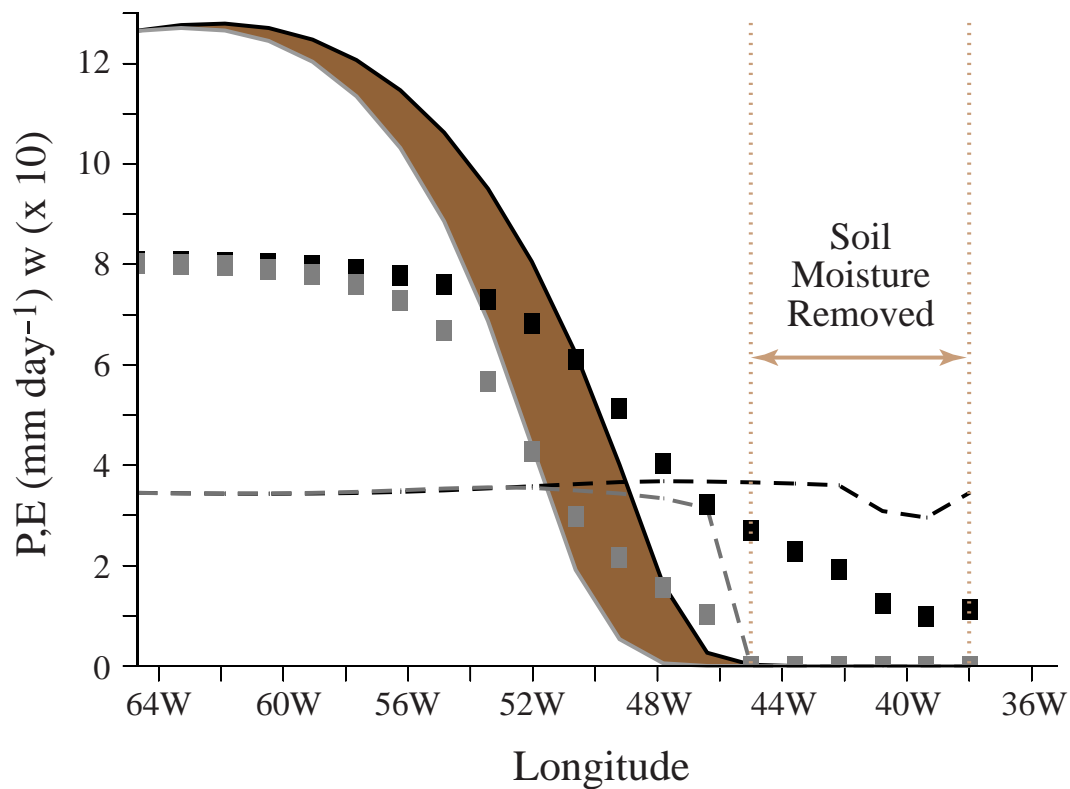


FIGURE 9: Zonal cross-sections of precipitation (solid lines), evaporation (dashed lines), and soil wetness (squares) for the standard full geometry QTCMI simulation (black) and the sensitivity simulation with soil moisture explicitly removed where $P = 0$ (gray). Results shown are averaged over pentads 50-54. The dashed vertical lines and light brown arrow indicate the region for which soil moisture is zeroed out in this averaging period. The dark brown shading highlights that the precipitation field is altered downstream of where the soil soil moisture is perturbed.